

See discussions, stats, and author profiles for this publication at: <https://www.researchgate.net/publication/282001612>

# INFLUENCE OF THE BOUNDARIES IN IMAGING FOR DAMAGE LOCALIZATION IN 1D DOMAINS

Conference Paper · July 2015

CITATION

1

READS

43

3 authors:



**Chrysoula Tsogka**

University of California, Merced

116 PUBLICATIONS 2,173 CITATIONS

[SEE PROFILE](#)



**Ioannis Petromichelakis**

Columbia University

13 PUBLICATIONS 28 CITATIONS

[SEE PROFILE](#)



**Christos Panagiotopoulos**

Foundation for Research and Technology - Hellas

42 PUBLICATIONS 482 CITATIONS

[SEE PROFILE](#)

Some of the authors of this publication are also working on these related projects:



Algorithmic Development and Analysis of Pioneer Techniques for Imaging with waVES [View project](#)



Symplegma: Java implementation for numerical methods in computational mechanics [View project](#)

## INFLUENCE OF THE BOUNDARIES IN IMAGING FOR DAMAGE LOCALIZATION IN 1D DOMAINS

Chrysoula Tsogka and Yiannis Petromichelakis and Christos G. Panagiotopoulos

Institute of Applied and Computational Mathematics  
Foundation for Research and Technology - Hellas  
Heraklion, GR-70013, Greece  
e-mail: tsogka@uoc.gr; web page: <http://www.tem.uoc.gr/> tsogka

**Keywords:** Time reversal, Kirchhoff migration, wave propagation, finite element techniques, defect localization

**Abstract:** *In the present work, we investigate the damage localization problem in 1D bounded domains and the influence of the boundaries in the quality of the image, using recordings at a limited number of spatial points as the input data. Based on the time reversal (TR) technique and utilizing the Green's function of the Helmholtz equation, the source localization problem is solved. This approach is then extended for the localization of defects given full knowledge of the domain in the undamaged state. For further analyzing the image, which suffers by inherent noise due to the presence of the boundaries, we utilize the modal expansion of the Green's function and propose different approaches for improving the quality of the image.*

### 1 INTRODUCTION

The detection and localization of defects based on recordings at limited number of spatial points, falls into the category of inverse problems which are usually ill-posed and hard to solve. A computational tool for solving a class of inverse wave (and/or vibration) problems is the time reversal (TR) technique which was originally introduced in [6] as a physical process. The principal idea behind TR is to send back in the medium the recorded signals but reversed in time. Due to the time-reversibility of the wave equation this process creates a back propagating wave that will focus at the original source location. A defect or damaged area, can be understood to act as a secondary source and therefore the principle of TR can be used to find its location. In this work we use time-reversal and migration imaging techniques in order to detect and localize the defect.

We assume here that we can measure the scattered field, that is the difference between the total field recorded in the presence of the defect and the incident field which corresponds to the healthy structure. In the context of the present work, these recordings are being produced numerically. Due to reflections from the boundaries the scattered field is complex and has multiple arrival time peaks. As a result, the quality of the image is degraded. Our objective is to investigate the influence of the boundaries and the total time of the experiment on the produced image.

### 2 SOURCE LOCALIZATION

In the present section we investigate the problem of localizing a source in an 1D bounded domain  $\Omega$  with the aid of one receiver that records the response at a point  $x_r$ . The source, excites one unknown point  $x_s$  (point source) according to a given excitation function  $f(t)$  which is a pulse emitted at a known time  $t_0$  (usually it is assumed that  $t_0 = 0$ ). Acoustic waves travel along the domain, reflect on the boundaries and the response  $p(x_r, t; x_s)$  is being recorded at the location of the receiver for a specified total time  $T$ .

The wave propagation process, that may be performed physically, is expressed by the following initial-boundary

value problem,

$$\begin{aligned} \frac{1}{c^2} \frac{\partial^2 p}{\partial t^2} - \frac{\partial^2 p}{\partial x^2} &= f(t) \delta(x - x_s), & (x, t) \in \Omega \times (0, T], \\ p(x, t) &= 0, & (x, t) \in \partial\Omega \times (0, T], \\ p(x, 0) = 0 \quad \text{and} \quad \frac{\partial p}{\partial t}(x, 0) &= 0, & x \in \Omega, \end{aligned} \quad (1)$$

which we solve numerically using a finite element method and we obtain the field  $p(x_r, t)$  at the location  $x_r$  of the receiver for  $t \in (0, T]$ . In Eq. (1),  $p$  is the displacement,  $c$  is the wave velocity assumed to be constant and  $\delta(x - x_s)$  is a delta function expressing the spatial distribution of the impulsive excitation. In the present work, we use a Ricker wavelet with central frequency  $f_0$  as the excitation function  $f(t)$ ,

$$f(t) = [1 - 2\pi^2 f_0^2 (t - t_0)^2] e^{-\pi^2 f_0^2 (t - t_0)^2}. \quad (2)$$

Additionally, instead of the delta function  $\delta(x - x_s)$ , in the numerical computations we use a spatial distribution of the source  $g(x - x_s)$ ,

$$g(x - x_s) = \begin{cases} \left[ \frac{1 - |x - x_s|^2}{r_0^2} \right]^3, & \text{for } |x - x_s| \leq r_0, \\ 0, & \text{for } |x - x_s| > r_0, \end{cases} \quad (3)$$

where  $\lambda_0$  is the central wavelength and  $r_0 = \frac{\lambda_0}{5}$ .

## 2.1 Time domain solution - TR

The principal idea in TR is to back-propagate the recorded signals reversed in time so as to achieve refocusing at the region of the source. For that purpose, the recorded signal  $p(x_r, t)$  is time reversed and re-transmitted from  $x_r$ . These time reversed waves, back-propagate through the medium and refocus on the position  $x_s$  of the source at a certain time  $t_{RF} = T - t_0$ , where  $t_0$  is the moment when the initial pulse was emitted from the source. The backward propagation step is expressed in terms of the acoustic field  $p^{TR}(x, t; x_r)$  by the initial-boundary value problem

$$\begin{aligned} \frac{1}{c^2} \frac{\partial^2 p^{TR}}{\partial t^2} - \frac{\partial^2 p^{TR}}{\partial x^2} &= p(x_r, T - t; x_s) \delta(x - x_r), & (x, t) \in \Omega \times (0, T], \\ p^{TR}(x, t) &= 0, & (x, t) \in \partial\Omega \times (0, T], \\ p^{TR}(x, 0) = 0 \quad \text{and} \quad \frac{\partial p^{TR}}{\partial t}(x, 0) &= 0, & x \in \Omega, \end{aligned} \quad (4)$$

which is numerically solved using the same finite element method. It is expected that  $p^{TR}(x, T - t_0; x_r)$  for  $x \in \Omega$ , will depict the location of the source.

## 2.2 Frequency domain solution - Imaging

In the present subsection, we solve the initial-boundary value problem in Eq. (4), i.e., the backward propagation step, in the frequency domain. For that purpose we express both the data at the receiver  $p(x_r, t; x_s)$  and the solution of the backward problem  $p^{TR}(x, t; x_r)$  with the aid of the Green's functions of the wave equation in the bounded domain  $\Omega$ ,  $G(x_s, x_r, t)$  and  $G(x_r, x, t)$  respectively as (see [2, 1])

$$\begin{aligned} p(x_r, t) &= f(t) \star_t G(x_s, x_r, t) & (5) \\ p^{TR}(x, t) &= F(x_r, t) \star_t G(x_r, x, t) & (6) \end{aligned}$$

where  $\star_t$  denotes Riemann convolution in time and  $F(x_r, t) = p(x_r, T - t)$  is the time reversed recorded signal. Eq. (5), is a model for the calculation of the data at the receiver. In practice we intent to measure the data physically or simulate it numerically and thus we do not need such a model but we write it for plenitude. Since it is easier to deal with convolutions in the frequency domain [1], we use the Fourier transform and the convolution theorem [4] to write the data at the receiver as

$$\widehat{p}(x_r, \omega) = \int_{-\infty}^{\infty} f(t) \star_t G(x_s, x_r, t) e^{i\omega t} dt = \widehat{f}(\omega) \widehat{G}(x_s, x_r, \omega) \quad (7)$$

and the time reversed data in the frequency domain  $\widehat{F}(x_r, \omega)$  as

$$\widehat{F}(x_r, \omega) = \int_{-\infty}^{\infty} p(x_r, T-t)e^{i\omega t} dt = \overline{\widehat{p}(x_r, \omega)}e^{i\omega T} = \overline{\widehat{f}(\omega)\widehat{G}(x_s, x_r, \omega)}e^{i\omega T} \quad (8)$$

where  $\widehat{G}(x_s, x, \omega)$  is the Green's function of the Helmholtz equation in  $\Omega$  and the overbar denotes complex conjugation. Additionally, the acoustic response during the backward step for  $x \in \Omega$  is

$$p^{TR}(x, t) = \frac{1}{2\pi} \int_{-\infty}^{\infty} \widehat{F}(x_r, \omega)\widehat{G}(x_r, x, \omega)e^{-i\omega t} d\omega = \frac{1}{2\pi} \int_{-\infty}^{\infty} \overline{\widehat{p}(x_r, \omega)}\widehat{G}(x_r, x, \omega)e^{i\omega(T-t)} d\omega \quad (9)$$

It is expected that a refocusing at the region of the source will take place at time  $t = t_{RF} = T - t_0$  and we thus define the imaging functional

$$\mathcal{I}(x) = p^{TR}(x, t = T-t_0) = \frac{1}{2\pi} \int_{-\infty}^{\infty} \overline{\widehat{p}(x_r, \omega)}\widehat{G}(x_r, x, \omega)e^{i\omega t_0} d\omega = \frac{1}{2\pi} \int_{-\infty}^{\infty} \overline{\widehat{f}(\omega)\widehat{G}(x_s, x_r, \omega)}\widehat{G}(x_r, x, \omega)e^{i\omega t_0} d\omega \quad (10)$$

and its numerical approximation by the midpoint rule assuming sufficiently small  $\Delta\omega$ 's

$$\mathcal{I}(x) = \frac{1}{2\pi} \sum_i \overline{\widehat{p}(x_r, \omega_i)}\widehat{G}^h(x_r, x, \omega_i)\Delta\omega_i \quad (11)$$

The quantity  $\widehat{G}^h(\xi, x, \omega)$  is an approximation of the term  $\widehat{G}(\xi, x, \omega)e^{i\omega t_0}$ , where  $\xi$  is a fixed point. It is the Fourier transform of  $G^h(\xi, x, t)$ , which is the numerically calculated response at  $x$  due to pulse emitted from  $\xi$  at time  $t_0$ .

### 2.3 Modal expansion

In order to investigate the behavior of the time reversal approach as well as the influence of the boundaries in the source localization process, we will utilize the eigenfunction (modal) expansion of the Green's function. For that purpose we make use of the expression in Eq. (7) for the data at the receiver and the approximation  $\widehat{G}^h$  of the Green's function, to write the imaging functional as

$$\mathcal{I}(x) = \frac{1}{2\pi} \sum_{\omega} \left| \widehat{f}(\omega) \right|^2 \overline{\widehat{G}(x_s, x_r, \omega)}\widehat{G}(x_r, x, \omega). \quad (12)$$

According to [5] the modal expansion formula for the Green's function of the Helmholtz equation in an 1D bounded domain is given by

$$G^{modal}(x, \xi, \omega) = \sum_{n=1}^N \frac{1}{\frac{\omega^2}{c^2} - \lambda_n} \Phi_n(x)\Phi_n(\xi), \quad (13)$$

where the  $\lambda_n$ 's and the  $\Phi_n$ 's are the eigenvalues and the eigenfunctions of the Laplace operator [5] respectively, while  $N$  is the total number of used eigenfunctions (modes). After plugging Eq. (13) into (12), neglecting the  $\widehat{f}(\omega)$ , and performing the calculations, we obtain

$$\tilde{\mathcal{I}}(x) = C_0 \sum_{i=1}^3 \left[ F_i \sum_{n=1}^N \sin\left(\frac{n\pi x}{L}\right) \sin\left(\frac{n\pi A_i}{L}\right) \right] \quad (14)$$

$i$	$F_i$	$A_i$
1	1.0	$x_s$
2	0.5	$x_s + 2x_r$
3	0.5	$x_s - 2x_r$

Table 1: Scale factors  $F_i$  and arguments  $A_i$ .

where the scale factors  $F_i$  and the arguments  $A_i$  are given in Table 1 while  $C_0$  is a constant that does not affect the image and can be omitted.

In order to obtain Eq. (14), careful attention should be taken for the frequency discretization to avoid resonances. For that purpose, the discrete  $\omega_i$ 's are chosen so that  $|\omega_{2i-1}^2 - c^2\lambda_i| = |\omega_{2i}^2 - c^2\lambda_i| = \text{constant}$  for all  $i$ 's, as shown in Figure 1.

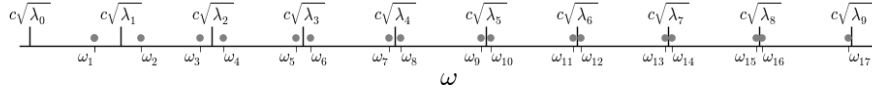
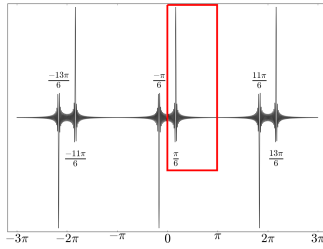
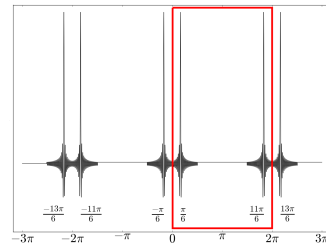


Figure 1: Discrete values  $\omega_i$ 's.

Finite series of products of two sines like the ones appearing in Eq. (14), have been investigated algebraically and numerically. It has been proved, that if the argument of the one sine is  $ny$  ( $y$  is the dependent variable) and the argument of the other sine is  $n\alpha$  ( $\alpha$  is an arbitrary constant value  $\neq k\pi, k \in \mathbb{N}$ ), the aforementioned series exhibits exactly one peak within the interval  $(0, \pi)$ . This can be indicatively seen in Figure 2a where the quantity  $P_{sin}(y, \alpha) = \sum_{n=0}^N \sin(ny) \sin(n\alpha)$  is plotted for  $\alpha = \frac{\pi}{6}$ .



(a)  $P_{sin}(y, \alpha) = \sum_{n=0}^N \sin(ny) \sin(n\alpha)$ ,  $\alpha = \frac{\pi}{6}$



(b)  $P_{cos}(y, \alpha) = \sum_{n=0}^N \cos(ny) \cos(n\alpha)$ ,  $\alpha = \frac{\pi}{6}$

Figure 2: Plots of  $P_{sin}$  and  $P_{cos}$  with  $N = 100$ .

Comparing the arguments of  $P_{sin}$  and of the series in Eq. (14), it can be seen that the latter exhibits exactly one peak in  $\Omega = [0, L]$ . Additionally, it has been proved that the limit of such a series as  $x$  approaches  $A_i$ , takes the constant value of  $\frac{N+1}{2}$ , given that the  $A_i$  is sufficiently far from any value  $kL$ , where  $k \in \mathbb{N}$ . These observations imply that the image for the source localization, contains one peak at the location of the source and another two, half-sized peaks. These smaller peaks, decrease the quality of the image and they are usually referred to as ghosts. They are caused by reflections on the boundaries of the domain and their locations depend on the positions of the source  $x_s$  and the receiver  $x_r$  (i.e., the arguments  $A_i$ ).

It can be observed, that the ratio between the height of the main peak which indicates the location of the source, and the maximum height of the ghost peaks, is 2.0. This ratio is referred to as *Signal to Noise Ratio* (SNR) and it is a measure of the quality of the image. One way to increase SNR in the present problem, is to increase the number of receivers. Due to the linearity of the imaging functional in Eq. (11), an image created by the recordings at  $N_r$  receivers, is equal to the superposition of the images for each one of the receivers alone. Making use of that property we can write

$$I(x) = \sum_{\omega} \sum_{r=1}^{N_r} \overline{\hat{p}(x_r, \omega)} \hat{G}^h(x_r, x, \omega). \quad (15)$$

It can be observed, that the SNR is linear with respect to the number of receivers and in this case it becomes  $2N_r$ .

### 3 DEFECT LOCALIZATION

In the previous section we presented the application of time reversal and imaging techniques for the localization of a source in an 1D bounded domain. In the present section we will extend this process in order to locate scatterers such as small defects. In this case, apart from the source (at  $x_s$ ) and the receiver (at  $x_r$ ), the 1D domain  $\Omega$  contains a small defect centered at  $x_d$ . The impulse emitted by the source, propagates, reflects on the boundaries and interacts with the defect (every time a wave reaches the defect it splits in a transmitted and a reflected component) while the receiver records the field  $p_{tot}(x_r, t)$  at  $x_r$  for a certain time  $T$ .

We assume in this case that we also know the incident field,  $p_{inc}(x, t)$ , which is the field in the healthy domain, i.e., the domain without the defect. It is possible then to compute the scattered field  $p_{scat} = p_{tot} - p_{inc}$ .

The fields at the receiver  $p_{inc}(x_r, t)$  and  $p_{tot}(x_r, t)$  may be measured physically, but in the present work we compute them numerically. Solving the initial-boundary value problem in Eq. (1) with a constant wave velocity  $c = c_{ref}$  results to  $p_{inc}$  while  $p_{tot}$  is obtained by solving the same problem but with the non-constant wave velocity field  $c(x)$ . If  $\Omega_d \subset \Omega$  is the small damaged area, then  $c(x) = c_d \neq c_{ref}$  for  $x \in \Omega_d$  and  $c(x) = c_{ref}$  otherwise.

It should be noted here that the scattered field  $p_{scat}$  of the defected domain, exhibits a major difference compared to the recorded field  $p(x, t; x_s)$  in the source localization problem of the previous section. The latter, contains only one pulse that propagates along the domain, reflects on a boundary and travels back towards the other boundary. This situation is the same independently from the total experiment time  $T$ . In the case of the defect however, the initial pulse, during its first passage from the defect, it splits into two pulses. One that passes by and another one that reflects back. These two pulses, reflect on the corresponding boundaries and each one splits into another two pulses when they pass over the defect. Conclusively, the defect acts as a multiple in time source and  $p_{scat}$  becomes more complicated as the total time  $T$  increases.

### 3.1 Time domain solution - TR

For the defect localization we apply TR numerically, equivalently to the case of the source, with the difference that it is the scattered field  $p_{scat}$  that is time reversed and re-transmitted from  $x_r$ . More specifically we solve the initial-boundary value problem in Eq. (4) with  $p_{scat}(x_r, T - t; x_s)$  instead of  $p(x_r, T - t; x_s)$ . The back-propagation of  $p_{scat}$ , is proved to provide better refocusing compared to the total field  $p_{tot}$ .

It should be noted, that due to the multiple emissions from the defect, there is not only one refocusing time, unlike the case of the source localization. It has been observed though, that the strongest refocusing is the one that corresponds to the original pulse, i.e., the first wavefront recorded. As a result, the refocusing time is  $t_{RF} = T - t_1 - t_0$ , where  $t_0$  is the time that the source emitted the original pulse and  $t_1 = \frac{|x_s - x_d|}{c_{ref}}$  is the travel time from the source to the defect. Conclusively,  $p(x, T - t_1 - t_0)$  for  $x \in \Omega$ , will depict the location of the defect.

### 3.2 Frequency domain solution - Imaging

Equivalently to the source localization process, in the present subsection we perform the backward step of the defect localization problem in the frequency domain. For that purpose we assume a model for our data, i.e., the scattered field at the receiver, that is known as the Born approximation [3] and is given by

$$\widehat{p}_{scat}(x_r, \omega) = k^2 \widehat{f}(\omega) \int_{\Omega_d} \widehat{G}(x_s, x, \omega) \widehat{G}(x, x_r, \omega) \rho(x) dx, \quad (16)$$

where  $k = \frac{\omega}{c_{ref}}$  is the wavenumber and  $\rho(x)$  the reflectivity of the defect defined as  $\rho = \frac{c_{ref}^2 - c_d^2}{c_d^2}$  for our example. For a point reflector located at  $x_d$  and with reflectivity  $\rho$  we get

$$\widehat{p}_{scat}(x_r, \omega) = k^2 \widehat{f}(\omega) \rho \widehat{G}(x_s, x_d, \omega) \widehat{G}(x_d, x_r, \omega). \quad (17)$$

According to [2] and based on this data model, it seems natural to define an imaging functional as

$$I(x) = \sum_{\omega} \overline{\widehat{p}_{scat}(x_r, \omega)} \widehat{G}^h(x_r, x, \omega) \widehat{G}^h(x, x_s, \omega). \quad (18)$$

It can be observed that in this approach, the reversed in time scattered field  $p_{scat}$  is back-propagated in two sub-steps. First, from the receiver  $x_r$  to a point  $x$  of the domain and second, from  $x$  to the source  $x_s$ . It might seem that the second sub-step (from  $x$  to  $x_s$ ) is redundant because it is the location of the defect that we are interested in, not the source. In fact, this sub-step is necessary, since to get a large contribution at the location of the defect we need to also account for the propagation from the source to the defect as suggested by the data model (Eq. (16)). Conclusively, Eq. (18) shows the appropriate imaging functional, equivalent to Eq. (11) but with the two Green's functions  $G(x_r, x, \omega)$  and  $G(x, x_s, \omega)$ . The appearance of these two Green's functions, differentiates imaging (in the frequency domain) from TR as described in Sec. 3.1, and for that reason the two approaches are not the same any more. It should be noted that this difference between the two approaches does not appear in the source localization.

### 3.3 Modal expansion

Equivalently to the source localization process, we will utilize the modal expansion of the Green's functions to achieve a deeper understanding of imaging for defect localization. Substituting,  $\widehat{G}^h$  and  $\widehat{p}_{scat}$  into Eq. (18), we obtain

$$I(x) = \sum_{\omega} k^2 \rho \left( \widehat{f}^h(\omega) \right)^2 \overline{\widehat{f}(\omega) \widehat{G}(x_s, x_d, \omega) \widehat{G}(x_d, x_r, \omega) \widehat{G}(x_r, x, \omega) \widehat{G}(x, x_s, \omega)}, \quad (19)$$

where  $\widehat{f}^h(\omega)$  is the Fourier transform of the excitation function used to calculate  $\widehat{G}^h$ . In general  $\widehat{f}^h(\omega)$  may be different from  $\widehat{f}(\omega)$  which is the excitation function of the forward problem.

Plugging the modal expansion formula in Eq. (13) into Eq. (19) and performing the calculations, we obtain the sum of series shown in Eq. (20).

$$\tilde{I}(x) = C_1 \left\{ \sum_{i=1}^{13} \left[ F_i \sum_{n=1}^N \cos\left(\frac{2n\pi x}{L}\right) \cos\left(\frac{2n\pi A_i}{L}\right) \right] + \sum_{n=1}^N \cos\left(\frac{n\pi x}{L}\right) \right\} + C_2, \quad (20)$$

where the scale factors  $F_i$  and the arguments  $A_i$  are given in Table 2 while  $C_1$  and  $C_2$  are constants that do not affect the image and can be omitted. Similarly to Sec. 2.3 we have neglected  $\widehat{f}(\omega)$ .

$i$	$F_i$	$A_i$	$i$	$F_i$	$A_i$	$i$	$F_i$	$A_i$	$i$	$F_i$	$A_i$
1	1.0	$x_d$	4	0.5	$x_d - x_s$	7	0.5	$x_d + x_r$	10	0.25	$x_d - x_s - x_r$
2	1.0	$x_s$	5	0.5	$x_d + x_s$	8	0.5	$x_s - x_r$	11	0.25	$x_d - x_s + x_r$
3	1.0	$x_r$	6	0.5	$x_d - x_r$	9	0.5	$x_s + x_r$	12	0.25	$x_d + x_s - x_r$
									13	0.25	$x_d + x_s + x_r$

Table 2: Scale factors  $F_i$  and arguments  $A_i$  of the image for defect localization.

The image in Eq. (20), is practically a sum of thirteen series each of which is a sum of products of two cosines. Such series have been investigated algebraically and numerically. It has been proved that if the argument of the one cosine is  $ny$  ( $y$  is the dependent variable) and the argument of the other cosine is  $n\alpha$  ( $\alpha$  is an arbitrary constant value  $\neq k\pi + \frac{\pi}{2}$ ,  $k \in \mathbb{N}$ ), the aforementioned series exhibit exactly two peaks within the interval  $(0, 2\pi)$  which are symmetrical with respect to the middle of the interval,  $\pi$ . This can be indicatively seen in Figure 2b where the quantity  $P_{cos}(y, \alpha) = \sum_{n=0}^N \cos(ny) \cos(n\alpha)$  is plotted for  $\alpha = \frac{\pi}{6}$ .

Comparing the arguments of  $P_{cos}$  and of the series in Eq. (20), it can be seen that the latter exhibits exactly two peaks in  $\Omega = [0, L]$  which are symmetrical with respect to  $\frac{L}{2}$ . Additionally, it has been proved that the limit of such a series as  $x$  approaches  $A_i$ , takes the constant value of  $\frac{N+1}{2}$ , given that the  $A_i$  is sufficiently far from any value  $kL$ , where  $k \in \mathbb{N}$ .

Conclusively, we expect a symmetric image that contains  $2 * 13 = 26$  peaks one of which should depict the defect. This is, one of the two symmetrical peaks that correspond to the argument  $A_i = x_d$ . The SNR of the image is 1.0, because the amplitude of the main peak that depicts the defect is the same with the amplitude of another 5 peaks which can be regarded as noise. The increase of the SNR is not possible, because in this approach the symmetry of the image can not be avoided. There will always be an equal peak at the defect and its symmetrical and we can not choose which one indicates the true defect location. We may though increase the quality of the image by increasing the number of receivers and sources. Due to the linearity of the imaging functional in Eq. (18), an image created by the recordings at  $N_r$  receivers due to  $N_s$  emitting sources, is equal to the superposition of the images for each one of the receivers and sources alone. Making use of that property we can write

$$I(x) = \sum_{\omega} \sum_{r=1}^{N_r} \sum_{s=1}^{N_s} \overline{\widehat{p}_{scat}(x_r, \omega) \widehat{G}^h(x_r, x, \omega) \widehat{G}^h(x, x_s, \omega)}. \quad (21)$$

In this way, each summand over the  $N_r$  receivers, will add a peak of a specific height at the location of the defect and another peak of the same height at the location of each receiver. As a result, the peak at the defect is amplified but not the other peaks because they are at different locations. The same holds for the sum over the sources, improving the quality of the image.

### 3.4 Total experiment time $T$

In TR for defect localization (Sec. 3.1) the choice of the total experiment time  $T$  is of significant importance. If  $T$  is multiple of  $\frac{L}{c_{ref}}$ , i.e., the wave travels many times along the length  $L$ , then  $p_{scat}$  is too complicated and the quality of the image degrades. Accordingly, the total time  $T$  that provides the best results is  $T = \frac{|x_s - x_d|}{c_{ref}} + \frac{|x_d - x_r|}{c_{ref}} + 2t_0$ , because this is the time where only the first wavefront is recorded. Due to the fact that  $x_d$  is not *a priori* known, a total time of  $T = \frac{2L}{c_{ref}} + 2t_0$  is the optimum choice. This is because it is sufficiently large for the pulse to travel from  $x_s$  to  $x_d$  and then to  $x_r$ , independently from the defect location and at the same time it is relatively small in order to achieve a good image quality.

In imaging (Sec. 3.2), the role of the total time  $T$  is similar to the TR case. This is because the terms in Eq. (18) are being calculated in the time domain and subsequently Fourier transformed. In modal expansion however, it is assumed that the total time is infinite. As a result, the two approaches are comparable, only if a sufficiently large  $T$  ( $\rightarrow \infty$ ) has been used for the calculation of the terms in Eq. (18).

## 4 NUMERICAL EXAMPLES

In the present section we present numerical results of TR and of the imaging techniques implemented on an 1D bounded domain of total length  $L = 30$  length units. The edges of the domain are subjected to the Dirichlet boundary conditions  $p(0, t) = p(L, t) = 0$  for both initial-boundary value problems Eqs. (1) and (4).

### 4.1 Source localization

Regarding the source localization problem, the three approaches, TR, imaging and imaging based on modal expansion have no fundamental difference and their results can be compared to each other. This is illustrated in Figure 3 where images calculated using the three approaches for a source at  $0.95L$  and a receiver at  $0.8L$  are plotted. The three lines agree almost perfectly.

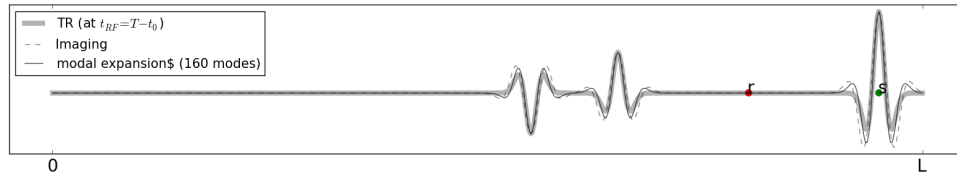
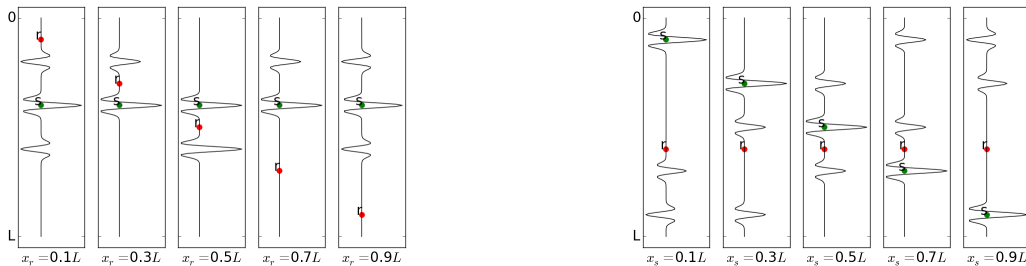


Figure 3: Comparison between TR, imaging and imaging based on modal expansion for a source at  $0.95L$  and a receiver at  $0.8L$ . There is very good agreement between the three methods.

The influence of the positions of the receiver and the source on the location of the ghost peaks, can be intuitively visualized in Figures 4a and 4b respectively. In Figure 4a, imaging results are shown for a source at the fixed position  $x_s = 0.4L$  and for different receiver locations. Figure 4b, shows imaging results as well but the receiver lies on the fixed position  $x_r = 0.6L$  while the source is at different locations.



(a) One source at  $x_s = 0.4L$  and different  $x_r$ 's.

(b) One receiver at  $x_r = 0.6L$  and different  $x_s$ 's.

Figure 4: Influence of the locations of the source and the receiver in imaging for source localization.

Observe in Figure 4a that for  $x_r = 0.3L$  and  $0.7L$  there is only one ghost. This can be explained by Eq. (14). For  $x_r = 0.3L$ , the argument  $x_s + 2x_r$  equals  $1.0L$  and therefore the corresponding sine and consequently the series that produces one of the two ghosts vanishes. Equivalently for  $x_r = 0.7L$  it holds  $x_s - 2x_r = -1.0L$ . For the same reason if we have a source at  $0.5L$  and a receiver at  $0.25L$ , we obtain an image without any ghost.

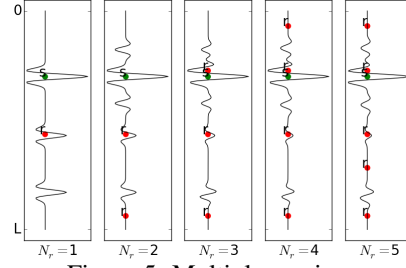
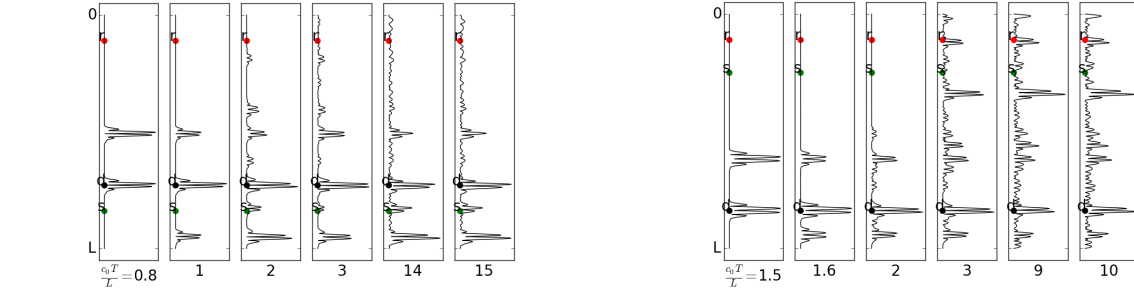


Figure 5: Multiple receivers

Figure 5, shows the improvement of the quality of the image for increasing number of receivers. More specifically, there is one source at a fixed location and one receiver is added at a random location in each sub-figure. It can be observed that the SNR is gradually increasing from 2.0 for one receiver to 10.0 for five receivers.

## 4.2 Defect localization

In the defect localization problem, TR exhibits significant differences (see Sec. 3.4) compared to the two imaging techniques and for that reason its results are being demonstrated separately.



(a) 1<sup>st</sup> TR example,  $x_s, x_r, x_d = 0.84L, 0.11L, 0.73L$ .

(b) 2<sup>nd</sup> TR example,  $x_s, x_r, x_d = 0.25L, 0.11L, 0.84L$ .

Figure 6: TR examples

Figure 6, shows TR results for two examples with increasing total experiment time. More specifically, in the first example there is a source at  $x_s = 0.84L$ , a receiver at  $x_r = 0.11L$  and the defect at  $x_d = 0.73L$  and in the second,  $x_s = 0.25L$ ,  $x_r = 0.11L$  and  $x_d = 0.84L$ . These images depict the backward propagating field at the refocusing time  $t_{RF} = T - \frac{|x_s - x_d|}{c_{ref}} - t_0$ .

In the 1<sup>st</sup> example (Figure 6a) for a total time of  $T = 0.8 \frac{L}{c_0}$ , the image exhibits a SNR of about 1.0, because there is one peak at the defect location and another one ghost peak of the same height that reduces the quality of the image. The total time  $T = 0.8 \frac{L}{c_0}$  corresponds to the time for which we expect the optimum image quality, i.e., approximately  $T = \frac{|x_s - x_d|}{c_{ref}} + \frac{|x_d - x_r|}{c_{ref}} + 2t_0$  as explained in Sec. 3.4, where  $c_0 = c_{ref}$ . It is interestingly observed though, that for  $T = 1.0 \frac{L}{c_0}$  the quality of the image is higher with a SNR of about 2.0. This is because in the latter case, apart from the first wavefront emitted by the defect, the receiver has recorded its reflection to the nearest boundary as well. This reflection has created a second ghost peak on the one hand, but it has amplified the main peak of the defect on the other, leading to the SNR of 2.0. The same exactly observation can be made in the 2<sup>nd</sup> TR example (Figure 6b) for  $T = 1.5 \frac{L}{c_0}$ . In both the TR examples, when increasing the total time  $T$  the quality of the image gradually reduces until it is stabilized to a SNR of about 1.0.

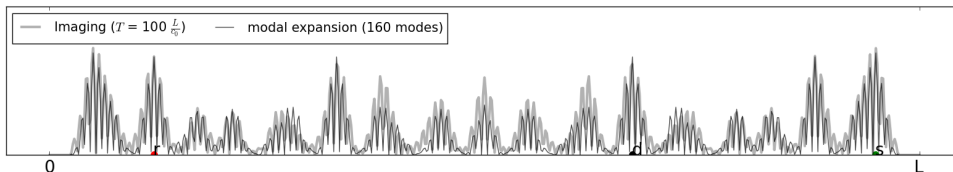


Figure 7: 1<sup>st</sup> Imaging example,  $x_s, x_r, x_d = 0.95L, 0.12L, 0.67L$ .

As mentioned in Sec. 3.4, imaging and TR are different approaches that can not be compared to each other. Additionally, imaging and modal expansion based imaging may be compared only if the total time for imaging approaches infinity. Accordingly, Figs. 7 and 8 show imaging for a total time of  $T = 100 \frac{L}{c_0}$  and modal expansion based imaging using 160 modes for two examples. In the first example (Figure 7) the source is located at  $x_s = 0.95L$ , the receiver at  $x_r = 0.12L$  and the defect at  $x_d = 0.67L$  while in the second example (Figure 8)  $x_s = 0.29L$ , the receiver at  $x_r = 0.23L$  and the defect at  $x_d = 0.87L$ . The two approaches are very close to each other.

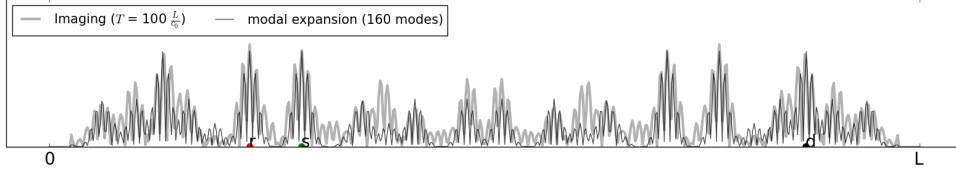


Figure 8: 2<sup>nd</sup> Imaging example,  $x_s, x_r, x_d = 0.29L, 0.23L, 0.87L$ .

The symmetry of the image with respect to the middle of the domain is present as expected. Moreover, there are six high peaks (three for the source the receiver and the defect and their symmetrical) of maximum height that lead to a SNR ratio of 1.0. The fact that the 13 peaks shown in Table 2 and their symmetrical are not clearly distinguished, is attributed to their large width, making them to mix up or to cancel out between each other.

It has been shown in equation (21), that the increase of the receivers and the sources improves the quality of the image. This is illustrated in Figure 9, where one receiver and one source are being alternately added at a random location in each sub-figure. The total number of receivers  $N_r$  and sources  $N_s$  is shown at the bottom of each image. Figure 9 clearly shows the gradual improvement of the quality of the image for increasing number of receivers and

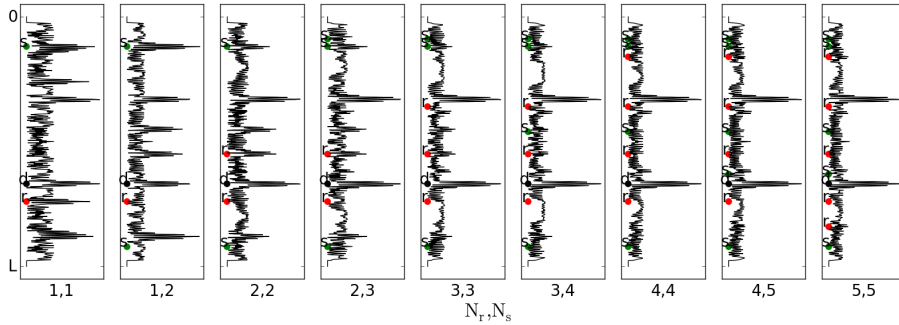


Figure 9: Imaging example with a defect at  $x_d = 0.67L$  and increasing  $N_r$  and  $N_s$ .

sources. In the final image, where  $N_r = N_s = 5$ , there are only two discrete peaks, one that indicates the true defect location and its symmetrical with respect to the middle of the image which has the same amplitude. This second peak is a ghost peak and is regarded as noise resulting to a SNR equal to 1.0, i.e., despite the obvious improvement of the image quality, the SNR does not improve. The only way to increase the SNR in imaging for defect localization is to reduce the total experiment time. This reduction can not be applied to the modal based imaging technique because in this case it is assumed that the total time is infinite. Figure 10 shows images for increasing total time  $T$ . It is obvious, that for short total times, there is only one clear peak indicating the true

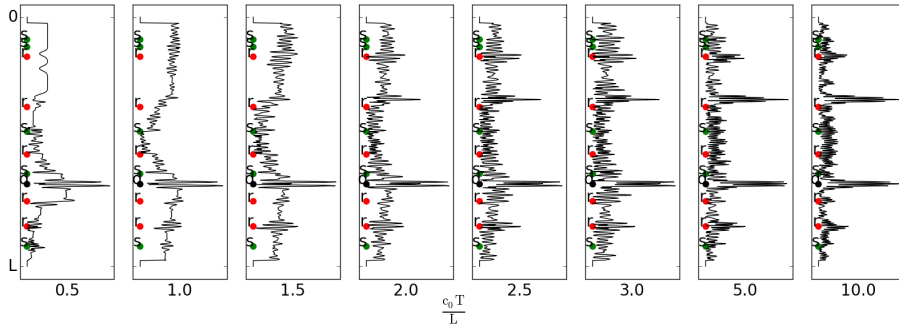


Figure 10: Imaging example with a defect at  $x_d = 0.67L$  and increasing total time  $T$ .

defect location. In the first sub-figure, for  $T = 0.5 \frac{L}{c_0}$  the SNR is about 4.0 and it gradually decreases until a value of 1.0 for  $T = 10.0 \frac{L}{c_0}$ .

### 4.3 2D Example

Despite the fact that the extension of the imaging technique described in Sec. 3.2 in two dimensional problems, is beyond the scope of the present work, we demonstrate some results indicatively. The defect localization problem is solved in a 2D bounded square domain  $\Omega$  of edge length  $L$  subjected to the Dirichlet boundary conditions  $p(x, t) = 0, x \in \partial\Omega$ . The domain contains one square shaped defect of width  $0.01L$  centered at  $(0.80L, 0.45L)$ , as well as, 20 sources and 20 receivers which are collocated and their locations have been randomly selected. Figure

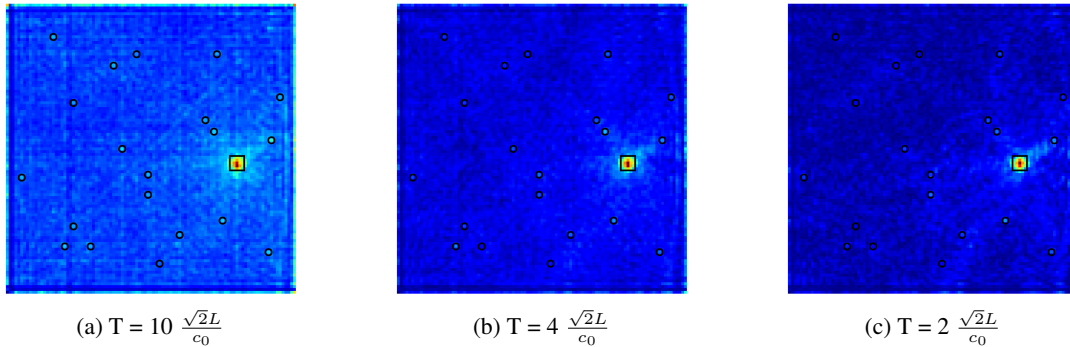


Figure 11: 2D Imaging example, one defect at  $(0.80L, 0.45L)$ , 20 receivers and 20 sources which are collocated.

11 shows the image for three different total experiment times. The total times used are multiples of the time that the wave needs to travel a distance equal to the diagonal of the 2D domain. It can be observed that for increasing total time, the quality of the image decreases. Additionally, it is obvious that 2D imaging produces significantly less noisy results compared to 1D imaging. This is mainly attributed to the fact that in 1D imaging the defect separates the domain in two different sub-domains, which does not hold in 2D imaging. As a result, the influence of the defect to the wave propagation process, is significantly higher in the 1D case. Moreover, the usage of a large number of sources and receivers, improves the SNR and accordingly the quality of the image.

## 5 CONCLUSIONS

In the present paper we presented a methodology for localizing small defects in 1D bounded domains based on recordings at a limited number of spatial points. The similarities and the disparities between the source and the defect localization problems have been appropriately exploited for the achievement of solutions to the second. Additionally, the noise developed by reflections on the boundaries, has been extensively analyzed and approaches for the improvement of the quality of the image have been proposed. Finally, results of a defect localization problem in a 2D bounded domain are being indicatively demonstrated and proved to be very promising.

## References

- [1] Liliana Borcea. Interferometric imaging and time reversal in random media. In Björn Engquist, editor, *Encyclopedia of Applied and Computational Mathematics*. Springer, 2011.
- [2] Liliana Borcea, George Papanicolaou, and Chrysoula Tsogka. Interferometric array imaging in clutter. *Inverse Problems*, 21(4):1419, 2005.
- [3] M. Born and E. Wolf. *Principles of optics*. Academic Press, New York, 1970.
- [4] Karl F. Graff. *Wave Motion in Elastic Solids*. Dover Publications, 1991.
- [5] Michael D. Greenberg. *Application of Green's functions in science and engineering*. Prentice-Hall, Englewood Cliffs New Jersey, 1971.
- [6] Claire Prada, Francois Wu, and Mathias Fink. The iterative time reversal mirror: A solution to self-focusing in the pulse echo mode. *The Journal of the Acoustical Society of America*, 90(2):1119–1129, 1991.